

# The SRG/eROSITA all-sky survey

## X-ray scaling relations of galaxy groups and clusters in the western Galactic hemisphere

M. E. Ramos-Ceja<sup>1,\*</sup>, L. Fiorino<sup>1,\*</sup>, E. Bulbul<sup>1</sup>, V. Ghirardini<sup>2,1</sup>, N. Clerc<sup>3</sup>, A. Liu<sup>4,1</sup>, J. S. Sanders<sup>1</sup>, Y. E. Bahar<sup>2,1</sup>,  
J. Dietl<sup>5</sup>, M. Kluge<sup>1</sup>, F. Pacaud<sup>5</sup>, E. Artis<sup>1</sup>, F. Balzer<sup>1</sup>, J. Comparat<sup>1</sup>, Z. Ding<sup>1</sup>, N. Malavasi<sup>1</sup>, A. Merloni<sup>1</sup>, T. Mistele<sup>1</sup>,  
K. Nandra<sup>1</sup>, R. Seppi<sup>6</sup>, S. Zelmer<sup>1</sup>, and X. Zhang<sup>1</sup>

<sup>1</sup> Max Planck Institute for extraterrestrial Physics, Giessenbachstrasse 1, 85748 Garching, Germany  
e-mail: mramos@mpe.mpg.de

<sup>2</sup> INAF, Osservatorio di Astrofisica e Scienza dello Spazio, Via Piero Gobetti 93/3, 40129, Bologna, Italy

<sup>3</sup> IRAP, Université de Toulouse, CNRS, UPS, CNES, Toulouse, France

<sup>4</sup> Institute for Frontiers in Astronomy and Astrophysics, Beijing Normal University, Beijing 102206, China

<sup>5</sup> Argelander-Institut für Astronomie (AIfA), Universität Bonn, Auf dem Hügel 71, 53121 Bonn, Germany

<sup>6</sup> Department of Astronomy, University of Geneva, Ch. d'Ecogia 16, CH-1290 Versoix, Switzerland

November 19, 2025

### ABSTRACT

The soft X-ray telescope on board the Spectrum-Roentgen-Gamma (SRG) mission, eROSITA (extended ROentgen Survey with an Imaging Telescope Array), has produced the largest sample to date of galaxy groups and clusters detected via their intracluster/intragroup medium (ICM/IGrM) emission. Scaling relations between the intrinsic properties of these systems provide valuable insight into their formation and evolution. In this work, we investigate the scaling relations between key physical properties, such as soft band X-ray luminosity, temperature, gas mass, and the low-scatter mass proxy  $Y_X$ , for the galaxy groups and clusters detected in the first eROSITA All-Sky Survey (eRASS1). Our analysis fully accounts for selection effects and the redshift evolution of the observable distributions. We construct a high-purity sample of 3061 galaxy groups and clusters spanning the redshift range  $0.05 < z < 1.07$  and mass range of  $1.1 \times 10^{13} < M_{500}/M_\odot < 1.6 \times 10^{15}$ . This represents the largest sample to date used for scaling relation analysis. The selection function, derived from state-of-the-art simulations of the eROSITA sky, is rigorously incorporated into our modeling. We report best-fit parameters – normalization, slope, redshift evolution, and intrinsic scatter – for a set of scaling relations:  $L_X - T$ ,  $L_X - M_{\text{gas}}$ ,  $L_X - Y_X$ , as well as the  $M_{\text{gas}} - T$  relation. Our best-fit models indicate that the slopes of the scaling relations deviate significantly from self-similar expectations, while the redshift evolution remains consistent with the self-similar model. The fits exhibit small statistical uncertainties, likely owing to the large sample size. Our results are in good agreement with previous observational studies that account for selection effects, as well as with simulations that incorporate non-gravitational physics.

**Key words.** surveys – galaxies: clusters: general – galaxies: clusters: intracluster medium – X-rays: galaxies: clusters

## 1. Introduction

Galaxy clusters and groups retain a substantial fraction of baryons within their potential wells. They originate at the highest peaks of the cosmic density field, where matter departs from the Hubble flow and collapses under gravity into progressively larger haloes. In the simplest framework, clusters and groups result from scale-free gravitational collapse of the highest peaks in the early Universe (e.g., Kravtsov & Borgani 2012). This scenario implies that haloes of different masses and redshifts are scaled versions of one another, an assumption known as the self-similar model (Kaiser 1986). Within this framework, observable cluster properties are expected to follow simple power-law scaling relations with total mass.

Scaling laws, encompassing both baryonic and non-baryonic components, have long served as a probe of the underlying cosmological model (e.g., Reiprich & Böhringer 2002; Vikhlinin et al. 2009; Mantz et al. 2010; Allen et al. 2011; Reichardt et al. 2013; Bulbul et al. 2019; Pratt et al. 2019; Ghirardini et al. 2024).

Besides being essential in cosmology, scaling relations provide constraints on the thermodynamic evolution of baryons in the intracluster/group medium (ICM/IGrM) and enable us to quantify the impact of non-gravitational processes (e.g., Ettori et al. 2004; Maughan 2007; Pratt et al. 2009; Sun et al. 2009; Vikhlinin et al. 2009; Mantz et al. 2010; Eckmiller et al. 2011; Kettula et al. 2015; Lovisari et al. 2015; Ghirardini et al. 2021; Bahar et al. 2022). Departures from self-similarity arise from mechanisms that alter the ICM/IGrM gas distribution, such as feedback (e.g., McNamara & Nulsen 2007; Fabian 2012; Gitti et al. 2012; Barnes et al. 2017), bulk and turbulent motions (e.g., Churazov et al. 2004; Zhuravleva et al. 2014), and galactic winds (e.g., Menci & Cavaliere 2000; Tozzi & Norman 2001). As a result, scaling relations are widely studied to measure these deviations and to identify low-scatter mass proxies for cosmological applications (Kravtsov et al. 2006). For instance, luminosity–mass relations in galaxy groups have been used to test the effects of active galactic nuclei (AGN) feedback (e.g., Sun et al. 2009; Eckmiller et al. 2011; Lovisari et al. 2015; Bahar et al. 2022, 2024), while relations involving other observables, such as lu-

\* These authors contributed equally to this work.

minosity with the Compton- $\gamma$  parameter or optical richness, are central to multi-wavelength studies of clusters (e.g., Zhang et al. 2011; Planck Collaboration et al. 2013; Ider Chitham et al. 2020; Ramos-Ceja et al. 2022; Kluge et al. 2024).

The soft X-ray telescope eROSITA (extended ROentgen Survey with an Imaging Telescope Array, Predehl et al. 2021), aboard the Spectrum-Roentgen-Gamma (SRG) mission (Sunyaev et al. 2021) was launched on July 13, 2019. With its large collecting area (1365 cm<sup>2</sup> at 1 keV) and moderate angular resolution ( $\sim 30''$  at 1.49 keV), eROSITA provides an unprecedented view of the X-ray sky. Its primary goal is to build the largest, well-characterized cluster samples, enabling cosmological constraints from cluster abundances that are complementary to CMB probes when combined with weak-lensing mass calibration (Merloni et al. 2012).

In this work, we use the largest ICM/IGrM-selected sample of galaxy clusters and groups from the first eROSITA All-Sky Survey (eRASS1) to date to study X-ray scaling relations among key observables. The sample spans three orders of magnitude in mass and four in luminosity (Bulbul et al. 2024). With this dataset, we constrain the influence of non-thermal processes on intrinsic cluster properties and establish links between galaxy groups, transitional systems, and massive clusters, fully exploiting the statistical power of the eROSITA catalogues (Kluge et al. 2024; Merloni et al. 2024). Previous analyses based on the smaller-area eROSITA Final Equatorial-Depth Survey (eFEDS) have provided valuable scaling relations but were limited by sample size (Liu et al. 2022; Bahar et al. 2022; Chiu et al. 2022). Here, we extend those studies by a factor of two in sample size and probe haloes down to  $1 \times 10^{13} M_{\odot}$ . In particular, we investigate the scaling relations of eRASS1 clusters and groups between soft band X-ray luminosity, temperature, gas mass, and the low-scatter mass proxy  $Y_X$ .

This paper is organised as follows. In Section 2, we describe the group and cluster sample selection, the data reduction, and analysis. In Section 3, we present the scaling relation fitting method and the selection function used in this work. X-ray scaling relations between the X-ray properties of the selected clusters are given in Section 4. We discuss our results in Section 5, and provide a summary of the presented work in Section 6.

Throughout this paper, we use a  $\Lambda$ CDM cosmology, characterized by parameters from Planck Collaboration et al. (2016), namely  $\Omega_m = 0.3089$ ,  $\sigma_8 = 0.8147$ ,  $H_0 = 67.74 \text{ km s}^{-1} \text{ Mpc}^{-1}$ , and  $n_s = 0.9667$ . Quoted error bars correspond to a  $1\sigma$  confidence level unless noted otherwise.

## 2. Sample Selection and Data Analysis

In this section, we present the selected cluster sample and the X-ray data analysis to extract its X-ray properties. The sample of sources and their X-ray properties are based on our previously published catalogues. We provide critical points on the sample selection and eROSITA X-ray analysis.

### 2.1. eROSITA galaxy clusters and groups sample

We base our analysis on the eROSITA primary galaxy cluster and group catalog presented in Bulbul et al. (2024) and Kluge et al. (2024). From the first all-sky survey of the Western Galactic hemisphere, this catalog reports 12,247 galaxy clusters with redshifts between 0.003 and 1.323 and extent likelihood  $\mathcal{L}_{\text{ext}} > 3$ . However, it is estimated to contain a contamination fraction exceeding  $> 14\%$ , primarily from background fluctuations and

misclassified AGN or other point-like sources (Seppi et al. 2022; Clerc et al. 2024; Kluge et al. 2024; Balzer et al. 2025).

To utilise a clean sample in our analysis, we apply strict cuts on the  $\mathcal{L}_{\text{ext}} > 12$ ,  $z > 0.05$ , and  $M_{500}^1 > 1 \times 10^{13} M_{\odot}$  (details of the mass determination are provided in Section 2.2). Additionally, we apply a `IN_ZVLIM == TRUE` flag to avoid shallow optical/NIR data where the false-positive rate is known to increase steeply (Kluge et al. 2024). The final sample<sup>2</sup> utilised in this work includes 3061 clusters of galaxies and galaxy groups in the redshift range of  $0.05 < z < 1.07$  with a median redshift of 0.25. The purity level of the sample is estimated to be  $\sim 98\%$ <sup>3</sup>. This sample covers a mass range of  $1.1 \times 10^{13} M_{\odot}$  to  $1.6 \times 10^{15} M_{\odot}$ , including 219 galaxy groups, i.e., systems with  $M_{500}$  below  $1 \times 10^{14} M_{\odot}$ . This study includes the largest number of galaxy groups analysed in the context of scaling relations. It comprehensively spans the mass range from low-mass galaxy groups to massive clusters. The redshift distribution of the sample is displayed in the left panel of Fig. 1, and the  $M_{500}$  cluster masses are shown on the right panel.

### 2.2. Data reduction and analysis

The X-ray properties of the clusters in our sample are extracted from Bulbul et al. (2024), following an eROSITA standard data reduction and analysis procedure. The event files were processed using the eROSITA Science Analysis Software System (eSASS; Brunner et al. 2022), with pipeline version 010 (Merloni et al. 2024). Images and exposure maps for each cluster were generated using the `evtool` and `expmap` commands.

To obtain the physical properties of each cluster, Bulbul et al. (2024) performed imaging analysis using the MultiBand Projector 2D<sup>4</sup> (MBProj2D; Sanders et al. 2018) tool. MBProj2D forward fits cluster images in multiple bands with physical models of clusters, including an electron density profile, a temperature profile, and even a metallicity profile if allowed by the data quality. During this process, a Markov chain Monte Carlo (MCMC) analysis is used to generate profiles of cluster physical quantities. When enough energy bands, particularly the hard band, are included in the fitting, MBProj2D can constrain the cluster temperature with comparable precision to spectral fitting. In the analysis of the eRASS1 clusters, Bulbul et al. (2024) used seven bands from 0.3 keV to 7 keV, and thus, were able to obtain temperature measurements for clusters when there were enough photons (Bulbul et al. 2024). Limited by the number of photons for most eRASS1 clusters, they adopt an isothermal model in the analysis. Therefore, only an average temperature is obtained for each cluster, rather than a temperature profile. Metallicity is fixed at  $0.3 Z_{\odot}$  globally, with solar abundances adopted from Asplund et al. (2009). The electron density profiles are described with the model from Vikhlinin et al. (2006), after discarding the second  $\beta$  component, which is used for fitting cluster outskirts. The other quantities and their probability distribution functions, such as the soft band X-ray luminosity (in the 0.5 – 2.0 keV energy band) and gas mass, are derived from the chain of free parameters in the density profile and temperature.

<sup>1</sup>  $M_{500}$  denotes the mass within  $R_{500}$ , defined as the radius enclosing a mean density equal to 500 times the critical density of the Universe at the cluster's redshift.

<sup>2</sup> Starting with 3414 systems ( $\mathcal{L}_{\text{ext}} > 12$ ), applying  $z > 0.05$  removes 146,  $M_{500} > 1 \times 10^{13} M_{\odot}$  removes 4 more, and `IN_ZVLIM = TRUE` excludes 203.

<sup>3</sup> The purity of the sample is obtained using Eq. 15 in Kluge et al. (2024).

<sup>4</sup> <https://github.com/jeremysanders/mbproj2d>

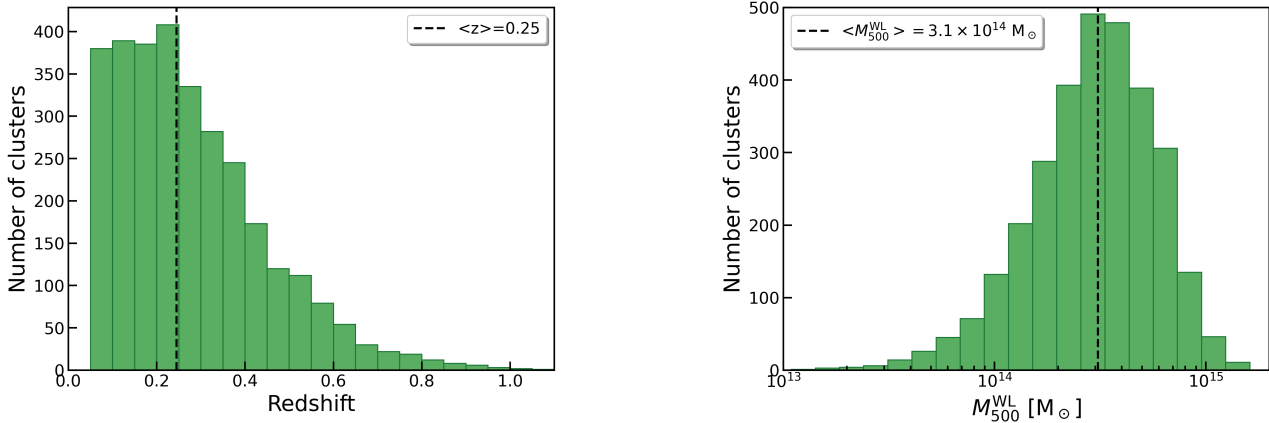


Fig. 1: Redshift (*left panel*) and mass distribution (*right panel*) of the 3061 eRASS1 clusters and groups used in this work. The median redshift and mass of the sample are shown by the vertical dashed black lines.

Due to the shallow nature of the eRASS1 survey, most eRASS1 clusters lack enough counts for precise temperature measurements. To assess temperature constraints, Bulbul et al. (2024) analyzed the MCMC chains, built logarithmic histograms of the temperature, and derived the marginal posterior distributions. Then, they computed the 98.7% ( $2.5\sigma$ ) highest density interval (HDI), reporting limits when the interval hits the parameter boundaries. In our sample of 3061 clusters, 2 only have upper limits and 1663 have lower limits on temperature. The remaining 1396 clusters have constrained temperatures, for which the model of the posterior distribution has been adopted as the best-fit temperatures, and the 68.2% HDI as the uncertainty range. For luminosity, only 17 clusters in our selected sample have upper-limit estimates, while the rest have constrained values. This does not represent a limitation for our scaling relation analysis, as the fitting procedure explicitly incorporates the full individual observable posterior distributions. In doing so, the method treats measurement uncertainties in a statistically rigorous way and ensures that the resulting relations remain robust and reliable (see Section 3.1). Even if the analysis were restricted to clusters with well-constrained temperatures, for example, by increasing the  $\mathcal{L}_{\text{ext}}$  threshold, determining the selection function would not be straightforward. In the eRASS1 digital twin, only a limited number of detections exceed  $\mathcal{L}_{\text{ext}} > 12$ , making it challenging to train the selection function (see Sect. 3.2 and Clerc et al. 2024).

In this work, we use the X-ray properties integrated over  $R_{500}$ , which is calculated from the  $M_{500}$  estimates.  $M_{500}$  is inferred using the scaling relations between mass and X-ray count rate, with the calibration by weak lensing shear profiles (Ghirardini et al. 2024; Grandis et al. 2024; Kleinebreil et al. 2024; Okabe et al. 2025). This scaling relation is calibrated using the weak lensing shear profiles from the Dark Energy Survey (DES), Kilo Degree Survey (KiDS), and HyperSupremeCam (Okabe et al. 2025).

### 3. Scaling Relation Modeling

In this work, we will follow the methods introduced by Bahar et al. (2022) to model the scaling relations of eROSITA-selected samples. To ensure a fair comparison between similarly selected samples, we employ the same form of scaling relations and likelihood fitting method. We briefly discuss the method in this section.

#### 3.1. Likelihood and fitting procedure

A simple form of scaling relations proposed by Kaiser (1986) relies on the purely gravitational collapse model, known as a self-similar relation. Assuming this model, one can derive the slope of the scaling relations; for example, the power-law index for the soft band X-ray luminosity ( $L_X$ ) and temperature ( $T$ ) is  $3/2$ , while the slope is 1 for the relation between  $L_X$  and gas mass ( $M_{\text{gas}}$ ).

We adopt the following general form of power-law relations between observables  $Y$  and  $X$ , taking into account both redshift and mass evolution:

$$\frac{Y}{Y_{\text{piv}}} = A \left( \frac{X}{X_{\text{piv}}} \right)^B \left( \frac{E(z)}{E(z_{\text{piv}})} \right)^C, \quad (1)$$

where  $Y_{\text{piv}}$  and  $X_{\text{piv}}$ ,  $z_{\text{piv}}$  are the pivot values of the observables  $Y$ ,  $X$ , and redshift of the sample.  $A$  is the normalization,  $B$  is the slope with respect to  $X$ , and  $C$  is the slope of the redshift evolution of the power-law relation (Bulbul et al. 2019; Bahar et al. 2022). X-ray scaling relations are expected to evolve with redshift, even in a purely gravitational scenario, due to cosmological expansion and the resulting change in the Universe's matter density. The redshift evolution is modeled using the evolution function, which is defined as  $E(z) = H(z)/H_0$ , where  $H(z)$  is the Hubble-Lemaître parameter and  $H_0$  is the Hubble constant. For all cases, we adopt a log-normal intrinsic scatter in the observables, denoted as  $\sigma_{Y|X}$ . For each scaling relation, we fit for four free parameters:  $A$ ,  $B$ ,  $C$ ,  $\sigma_{Y|X}$ . We also provide the best-fit scaling relations, assuming a self-similar evolution of the derived quantities in this work.

Bahar et al. (2022) modeled the scaling relation between galaxy cluster observables by constructing a comprehensive likelihood function that incorporates selection effects, measurement uncertainties, and the underlying cosmological distribution of clusters. The full likelihood accounts for the detection probability of a cluster, the correlation in measurement uncertainties, and the intrinsic scatter in the scaling relation, all evaluated at a fixed cosmology, self-consistently obtained from eROSITA cluster number counts (Ghirardini et al. 2024). Given the high precision of spectroscopic and photometric redshift determinations ( $\delta z/(1+z) \leq 0.005$  in  $0.05 < z < 0.9$ ) in the eRASS1 sample, we also treat the cluster redshifts as known and neglect their uncertainties in our analysis (Kluge et al. 2024). The instrumental

effects, such as varying exposure time and telescope characteristics, are taken into account in the selection function (see Section 3.2).

As mentioned before, the observable–observable scaling relations are modeled as a log-normal distribution around a power-law form, and the cosmological distribution of the lower-level observable is derived by convolving the mass function with a mass–observable scaling relation calibrated via weak lensing. With these components, we marginalize over the true values of the observables to obtain the likelihood of the measured two observables  $X$  and  $Y$  for a given cluster:

$$P(\hat{Y}, \hat{X}, I|\theta, z, S) = \iint_{Y, X} P(I|Y, z, S) P(\hat{Y}, \hat{X}|Y, X) \times P(Y|X, \theta, z) P(X|z) dY dX, \quad (2)$$

where  $P(I|Y, z, S)$  is the probability ( $I$ ) of a cluster being included in our sample, i.e., the selection function;  $P(\hat{Y}, \hat{X}|Y, X)$  is the two-dimensional measurement uncertainty (correlation) of the observables;  $P(Y|X, \theta, z)$  models the  $Y - X$  scaling relation; and  $P(X|z)$  represents the cosmological distribution of the observable  $X$ . The variable  $\theta$  contains the free parameters of the scaling relation:  $A$ ,  $B$ ,  $C$ , and the scatter  $\sigma_{Y|X}$ .

In contrast with Bahar et al. (2022) and following Ghirardini et al. (2024) and Sanders (A&A submitted 2025), the cluster sky position,  $S$ , is included in the likelihood and the selection function. This is due to the eRASS1 survey strategy, which results in position-dependent exposure times, with significantly deeper coverage near the ecliptic poles (Predehl et al. 2021). Additional sky-position-dependent effects, such as galactic absorption (HI4PI Collaboration et al. 2016; Willingale et al. 2013), detector response, and background levels (Freyberg et al. 2021), are also considered in the analysis, as they impact the cluster detection efficiency and count-rate measurements.

As in Bahar et al. (2022), to mitigate the sensitivity to cosmological assumptions and the exact form of the mass-observable relation, we do not use the observed number of clusters as data. Instead, we treat the number of detections as a model-dependent quantity and construct the cluster likelihood using Bayes' theorem. This approach allows us to focus on constraining the scaling relation parameters while avoiding terms that depend explicitly on cosmological volume or completeness corrections, enhancing the robustness of our fits under a fixed cosmological model. This likelihood modeling is similar to the method presented in Giles et al. (2016) and Pacaud et al. (2016). We derive the cosmological distribution of the observable  $X$  as a function of redshift for a fixed cosmology ( $P(X|z)$ ) and an assumed  $X - M$  scaling relation. We transform the Tinker et al. (2008) mass function into an “ $X$ -function.” This conversion is performed using the weak-lensing mass-calibrated scaling relations of Chiu et al. (2022) (see Bahar et al. 2022, for further details).

Finally, we used the Bayes theorem to obtain the likelihood of our clusters being detected given the measured X-ray observables,

$$\mathcal{L}(\hat{Y}_i, \hat{X}_i|I, \theta, z_i, S_i) = \frac{P(\hat{Y}_i, \hat{X}_i, I|\theta, z_i, S_i)}{\iint_{\hat{Y}_i, \hat{X}_i} P(\hat{Y}_i, \hat{X}_i, I|\theta, z_i, S_i) d\hat{Y}_i d\hat{X}_i}. \quad (3)$$

The final total likelihood is computed by multiplying the likelihood for all the individual clusters in the sample.

We fit the X-ray scaling relations using the emcee MCMC sampler (Foreman-Mackey et al. 2013) with the likelihood described above. We fit the eRASS1 cluster sample using flat priors:  $\mathcal{U}(0.1, 4)$  for the normalization  $A$ ,  $\mathcal{U}(-10, 10)$  for the slope

Table 1: Pivot values of the observables obtained for the galaxy group and cluster sample used in this work. The values represent the median value of the sample.

| X-ray observable | Median value                              |
|------------------|---|
| $z$              | 0.25                                      |
| $L_X$            | $6.53 \times 10^{43}$ erg s <sup>-1</sup> |
| $T$              | 2.27 keV                                  |
| $M_{\text{gas}}$ | $2.28 \times 10^{13}$ M <sub>⊙</sub>      |
| $Y_X$            | $4.94 \times 10^{13}$ M <sub>⊙</sub> keV  |

$B$ ,  $\mathcal{U}(-10, 10)$  for the redshift evolution  $C$ , and  $\mathcal{U}(0.1, 3.0)$  for the intrinsic scatter  $\sigma_{Y|X}$ . Pivot values correspond to the median of the observables (see Table 1). Each scaling relation is fit twice: once with  $C$ , the slope of the redshift evolution, as a free parameter, and once with  $C$  fixed to the self-similar expectation.

### 3.2. Selection function

A proper scaling relation fitting depends heavily on the accurate knowledge of the selection effects, such as the survey's incompleteness and contamination. The selection function model  $P(I|Y, z, S)$ , adopted here, closely follows the approach of Ghirardini et al. (2024) and is based on multiple mock realizations of the eROSITA all-sky survey (Seppi et al. 2022; Clerc et al. 2024). These simulations are designed to replicate the key instrumental characteristics of eROSITA, including exposure inhomogeneities, point-spread function variations, effective area changes, and the grasps of all seven telescopes. Foreground and background sources, such as stars, AGN, and galaxy clusters, are embedded within a full-sky light-cone N-body simulation (Comparat et al. 2020). AGN properties are assigned using abundance-matching techniques, while the emissivity profiles of galaxy clusters and groups are drawn from an observational template library, with associations based on halo mass, redshift, and dynamical state.

Source detection in the mock eRASS1 data follows the procedure detailed in Seppi et al. (2022). Detected sources are matched to simulated ones in the sky by considering spatial proximity, extent, and brightness, favoring associations with the brightest candidate in cases of ambiguity. Successful matches are flagged as true detections. This process produces a labelled dataset from which detection probabilities can be estimated across a broad range of cluster properties.

The modeling of detection probabilities is performed using Gaussian Process (GP) classifiers, trained on two-thirds of the matched simulated sample (Clerc et al. 2024). These non-parametric models interpolate the detection probability across the multi-dimensional space defined by cluster properties, such as soft band luminosity, redshift, and local exposure, with the optional inclusion of central emission measure. The remaining parameters are marginalized over, assuming the simulations capture their statistical distributions. Compared to spline interpolation, GP classifiers offer a more rigorous handling of uncertainty, particularly in sparsely sampled regions of parameter space. Model calibration is verified by checking that the predicted detection probabilities agree with the actual detection rates in the test set.

The selection function used in this work follows the cluster selection described in Sect. 2.1. It includes extended sources with  $\mathcal{L}_{\text{ext}} > 12$ , a simulated redshift range of  $0 \leq z \leq 1.5$ , and

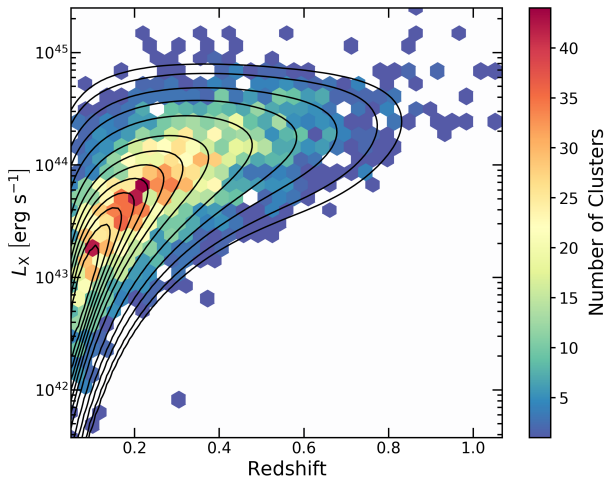


Fig. 2: Hexbin plot of the soft band X-ray luminosity (0.5 – 2.0 keV energy band) and redshift distribution of the selected 3061 eRASS1 clusters. Solid black curves show the PDF of the hypothetical  $L_X - z$  distribution given by the selection function (see Section 3.2 for details).

a lower mass limit of  $M_{500} = 1 \times 10^{13} M_{\odot}$ . In addition, sources are required to satisfy `IN_XGOOD==True`, a spatial mask from the optical identification that is connected to the `IN_ZVLIM` flag (see Sect. 2.1 and Kluge et al. 2024).

As in Bahar et al. (2022), to evaluate the performance and realism of the selection function, we compare the modeled luminosity distribution of detected clusters with observations. Specifically, we compute  $P(I, L_X, z, S) = P(I|L_X, z, S)P(L_X|z)P(z)$ , where  $P(L_X|z)$  is obtained using Eq. 6 in Bahar et al. (2022) together with the best-fit  $L_X - M$  relation from Chiu et al. (2022) and the Tinker et al. (2008) mass function; and  $P(z)$  is proportional to the comoving volume element  $dV_c(z)$ , assuming a constant comoving cluster density in the redshift range  $0 < z < 1.1$ . The comparison, shown in Fig. 2, demonstrates strong agreement between the observed (hexbin plot) and modeled (contours) soft band X-ray luminosity–redshift distributions, supporting the reliability and representativeness of the selection function within the eRASS1 survey context.

## 4. Results

In this section, we study the scaling relations between X-ray observables of securely detected eRASS1 clusters of galaxies. As mentioned in Section 1, X-ray observable scaling relations studies helps to understand the intracluster medium physics of galaxy groups and clusters. This work shows the  $L_X - T$ ,  $L_X - M_{\text{gas}}$ ,  $L_X - Y_X$ , and,  $M_{\text{gas}} - T$  scaling relations. A comparison with previous scaling relation results is also shown.

In contrast with Bahar et al. (2022), we do not include scaling relations that involve the bolometric luminosity. The reason is that, from eROSITA data, we are measuring the soft band luminosity directly, as determined in the standard eROSITA 0.2 – 2.3 keV energy band. The conversion from soft band to bolometric luminosity depends highly on the temperature and its uncertainty. Moreover, the used selection function is ultimately determined by the distribution of photon events in the soft band. Since the selection function is calibrated on simulations, all steps connecting the soft band event distribution to the bolometric luminosity are inherently model-dependent. Consequently, the selection function is sensitive to the assumptions adopted in the

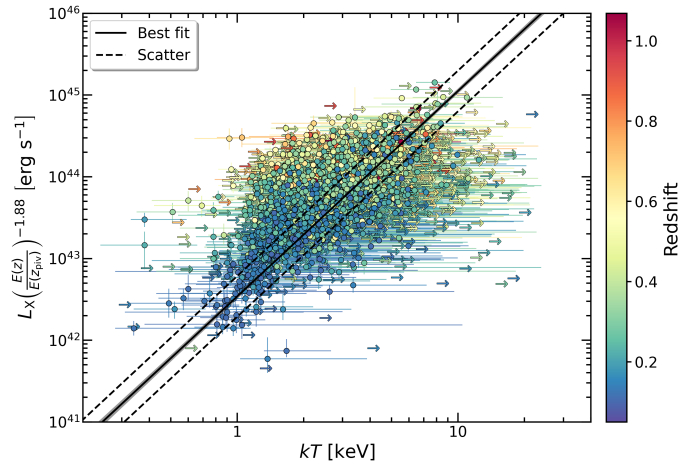


Fig. 3: Soft band (0.5 – 2.0 keV energy band) X-ray luminosity–Temperature,  $L_X - T$ , scaling relation of the selected galaxy group and cluster eRASS1 sample. Data points are color-coded according to their redshift. Arrows indicate temperature lower limits for objects in the sample with poorly constrained temperatures. The black line shows the best-fit scaling relation model. The black shaded area indicates the  $1\sigma$  uncertainty of the mean of the log-normal model, and the dashed black lines indicate the best-fit standard deviation ( $\sigma_{L_X/T}$ ) around the mean.

digital twin, which adds another layer of uncertainty in the analysis.

Table 2 presents the best-fit results for all scaling relations from both analyses, considering cases with the slope of the redshift evolution,  $C$ , left free, as well as fixed to the self-similar value. Appendix A provides the marginalized and joint posterior distributions of the model parameters for all scaling relation fittings.

### 4.1. Soft band X-ray luminosity–Temperature scaling relation

The soft band X-ray luminosity–temperature,  $L_X - T$ , relation is one of the most extensively studied among X-ray scaling relations, due to the relatively straightforward and almost independent measurement of both quantities using X-ray data. Both quantities probe different, yet intrinsically connected, aspects of the ICM: luminosity depends on the square of the electron density, making it highly sensitive to the spatial distribution of the hot gas, while temperature reflects the average kinetic energy of the ICM.

Previous studies revealed that the observed  $L_X - T$  relation does not follow the expected self-similar scaling ( $L_X \propto T^{3/2}$ ) derived from purely gravitational heating processes (; e.g., Markevitch 1998; Ettori et al. 2004; Pratt et al. 2009; Eckmiller et al. 2011; Maughan et al. 2012; Hilton et al. 2012; Kettula et al. 2015; Lovisari et al. 2015; Giles et al. 2016; Bahar et al. 2022). Although the precise slope varies across studies, due to factors like modeling approaches, sample selection, and calibration, there is a general consensus that the relation has a slope between 2.3 and 3.0. Numerous observational studies have consistently confirmed this deviation and attributed it to additional, non-gravitational physical processes (for reviews see Giodini et al. 2013; Lovisari & Maughan 2022). Therefore, a deeper understanding of the  $L_X - T$  relation can offer valuable insights into the thermal history of galaxy clusters.

Table 2: Best-fit parameters of the scaling relations. The fitted relation is of the form  $\frac{Y}{Y_{\text{piv}}} = A \left( \frac{X}{X_{\text{piv}}} \right)^B \left( \frac{E(z)}{E(z_{\text{piv}})} \right)^C$ , with a log-normal scatter of  $\sigma_{Y|X}$ . The fitting is performed twice: with a free redshift evolution (exponent  $C$ ), and with a redshift evolution fixed to the self-similar expectation. The displayed errors are  $1\sigma$  uncertainties obtained from the MCMC chains.

| Scaling relation |                  | Free redshift evolution   |                           |                         |                           | Self-similar redshift evolution |                           |                 |                           |
|------------------|------------------|---------------------------|---------------------------|-------------------------|---------------------------|---------------------------------|---------------------------|-----------------|---------------------------|
| $Y$              | $X$              | $A$                       | $B$                       | $C$                     | $\sigma_{Y X}$            | $A$                             | $B$                       | $C_{\text{SS}}$ | $\sigma_{Y X}$            |
| $L_X$            | $T$              | $0.41^{+0.02}_{-0.02}$    | $2.51^{+0.04}_{-0.04}$    | $1.88^{+0.34}_{-0.37}$  | $0.57^{+0.03}_{-0.03}$    | $0.39^{+0.02}_{-0.02}$          | $2.54^{+0.04}_{-0.03}$    | 1               | $0.60^{+0.03}_{-0.03}$    |
| $L_X$            | $M_{\text{gas}}$ | $0.988^{+0.006}_{-0.006}$ | $1.234^{+0.006}_{-0.006}$ | $2.16^{+0.07}_{-0.07}$  | $0.188^{+0.005}_{-0.005}$ | $0.988^{+0.005}_{-0.005}$       | $1.241^{+0.006}_{-0.006}$ | 2               | $0.190^{+0.005}_{-0.005}$ |
| $L_X$            | $Y_X$            | $0.86^{+0.01}_{-0.01}$    | $0.855^{+0.009}_{-0.009}$ | $2.09^{+0.16}_{-0.17}$  | $0.25^{+0.01}_{-0.01}$    | $0.85^{+0.01}_{-0.01}$          | $0.866^{+0.008}_{-0.008}$ | 8/5             | $0.27^{+0.01}_{-0.01}$    |
| $M_{\text{gas}}$ | $T$              | $0.44^{+0.02}_{-0.02}$    | $2.24^{+0.03}_{-0.03}$    | $-1.00^{+0.29}_{-0.30}$ | $0.49^{+0.02}_{-0.02}$    | $0.44^{+0.02}_{-0.02}$          | $2.22^{+0.03}_{-0.03}$    | -1              | $0.48^{+0.02}_{-0.02}$    |

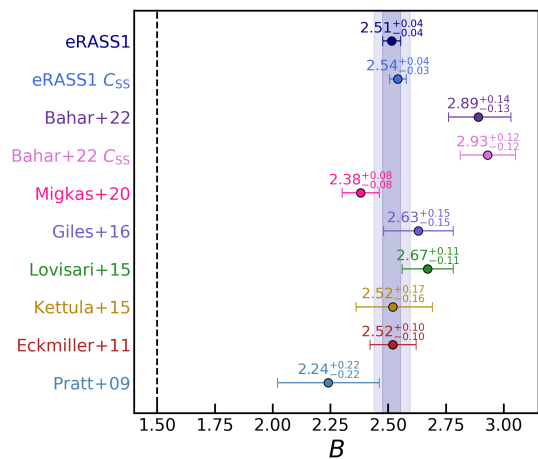


Fig. 4: Comparison of the slope  $B$  for the  $L_X - T$  scaling relation with literature results from Bahar et al. (2022, eFEDS cluster sample), Migkas et al. (2020), Giles et al. (2016, XXL cluster sample), Lovisari et al. (2015), Kettula et al. (2015), Eckmiller et al. (2011), and Pratt et al. (2009). All the shown errors are at the  $1\sigma$  level. The vertical shaded areas represent our best-fit measurements at the  $1-2\sigma$  confidence level. The vertical dashed black line display the self-similar expected value.

Our best-fit parameters for the  $L_X - T$  scaling relation are: a slope of  $B = 2.51^{+0.04}_{-0.04}$ , a redshift evolution parameter of  $C = 1.88^{+0.34}_{-0.37}$ , and an intrinsic scatter of  $\sigma_{L_X|T} = 0.57^{+0.03}_{-0.03}$ . Fig. 3 shows the corresponding best-fit model. Our best-fit slope,  $B$ , significantly deviates from the expected self-similar value ( $\sim 25\sigma$ ). However, it is consistent with most previous studies within  $1\sigma$  (see Fig. 4), except for the result from Bahar et al. (2022),  $B = 2.89^{+0.14}_{-0.13}$ , which shows a discrepancy at the  $\sim 2.6\sigma$  level. The group and cluster sample used in this work is significantly larger than those in previous studies, resulting in much smaller uncertainties on our best-fit parameters and placing tight constraints on them.

The discrepancy with Bahar et al. (2022) may be attributed to the larger fraction of galaxy groups in their sample. Several studies have found that the slope  $B$  of the  $L_X - T$  scaling relation of galaxy groups (systems with  $kT < 3.5$  keV) is steeper than the one for galaxy clusters, a difference attributed to their shallower potential wells and the stronger influence of non-gravitational processes (e.g., Maughan et al. 2012). In Bahar et al. (2022), 26% of their sample are groups with masses below  $< 10^{14} M_{\odot}$ , compared to only  $\sim 7\%$  in our analysis. This difference arises from the deeper eFEDS data used in their study, which allows

for the detection of lower-mass systems more effectively than the eRASS1 observations used here. Therefore, they obtain a steeper slope, potentially reflecting the underlying sample selection effects. In Section 5.2, we discuss further the impact of galaxy groups on the scaling relation fitting.

Our results show that the redshift evolution parameter is consistent with the self-similar expectation for temporal evolution ( $C_{\text{SS}} = 1$ ), showing an agreement at the  $\sim 2.4\sigma$  level. Giles et al. (2016), analyzing the 100 brightest clusters in the XXL Survey, reported  $C = 1.64^{+0.77}_{-0.77}$ , which is consistent with our result. Fixing the evolution parameter to its self-similar value yields a slope of  $B = 2.54^{+0.04}_{-0.03}$ , which is fully consistent with the case where evolution is left free. However, this slope is shallower than the value reported by Bahar et al. (2022),  $B = 2.93^{+0.12}_{-0.12}$ . The intrinsic scatter best-fit obtained in this work agrees well within  $2\sigma$  with the ones published previously by different authors, except for the ones from Bahar et al. (2022). Fig. B.1 shows a comparison of the intrinsic scatter  $\sigma_{L_X|T}$  with literature results. Our  $\sigma_{L_X|T}$  results agree within  $1\sigma$ , with previous studies (e.g., Pratt et al. 2009; Eckmiller et al. 2011; Lovisari et al. 2015; Giles et al. 2016), however, it is shallower than the value obtained by Bahar et al. (2022).

#### 4.2. Soft band X-ray luminosity–Gas mass scaling relation

X-ray luminosity and gas mass are intrinsically correlated observables, primarily due to their mutual dependence on the intracluster/group electron density. As a result, a strong statistical correlation is expected between them. A precise characterization of this correlation must account for selection biases, the underlying halo mass function, and use a statistically significant sample.

Most previous studies of the  $L_X - M_{\text{gas}}$  relation show a slight deviation from the self-similar expectations with respect to  $M_{\text{gas}}$  ( $L_X \propto M_{\text{gas}}$ ). The results vary across studies, with differences attributed to variations in modeling approaches, sample selection, and calibration (e.g., Zhang et al. 2011; Pratt et al. 2009; Lovisari et al. 2015; Mantz et al. 2016; Bahar et al. 2022).

Our best-fit parameters for the  $L_X - M_{\text{gas}}$  scaling relation are: a slope of  $B = 1.234^{+0.006}_{-0.006}$ , a redshift evolution parameter of  $C = 2.16^{+0.07}_{-0.07}$ , and an intrinsic scatter of  $\sigma_{L_X|M_{\text{gas}}} = 0.188^{+0.005}_{-0.005}$ . This best-fit model is presented in Fig. 5. Our best-fit slope is steeper and statistically inconsistent with the self-similar expectation ( $\sim 23\sigma$ ), while the redshift evolution parameter slope is consistent with the self-similar model ( $C_{\text{SS}} = 2$ ) at  $\sim 2\sigma$ . The significantly larger sample considered in this work allows for tighter constraints on the  $L_X - M_{\text{gas}}$  relation. By fixing the redshift evolution exponent to the self-similar value, the slope does not significantly change,  $B = 1.241^{+0.006}_{-0.006}$ .

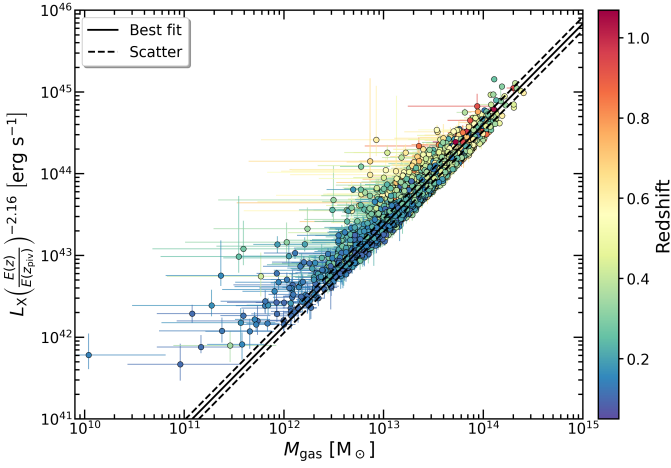


Fig. 5: Same as Fig. 3, but for soft band (0.5 – 2.0 keV energy band) X-ray luminosity–Gas mass,  $L_X - M_{\text{gas}}$ , scaling relation.

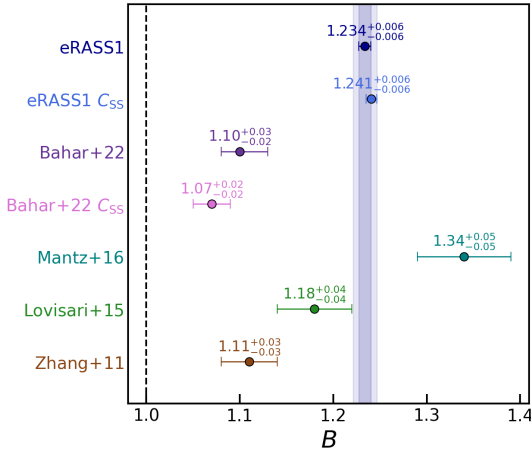


Fig. 6: Same as Fig. 4, but showing the slope  $B$  comparison of the  $L_X - M_{\text{gas}}$  scaling relation, including results from Bahar et al. (2022, eFEDS cluster sample), Mantz et al. (2016), Lovisari et al. (2015), and Zhang et al. (2011).

Fig. 6 compares our best-fit slope results with previous studies, considering both the self-similar and non-self-similar cases. Our findings are consistent within  $2\sigma$  with studies that include high-mass systems; for example, Lovisari et al. (2015) and Mantz et al. (2016), which both include massive, luminous clusters, report slopes steeper than the self-similar expectation. In contrast, studies that focus on or include a significant fraction of galaxy groups tend to find shallower slopes (e.g., Zhang et al. 2011; Bahar et al. 2022). This trend is also evident in the group-only analysis by Lovisari et al. (2015), who report a slope of  $B = 1.18^{+0.04}_{-0.04}$ . As noted by Bahar et al. (2022), only a few studies have reported the intrinsic scatter of the  $L_X - M_{\text{gas}}$  relation. Fig. B.2 presents a comparison between our measured  $\sigma_{L_X|M_{\text{gas}}} = 0.188^{+0.005}_{-0.005}$  and values from the literature. We find significant tension with previous results, at the  $\sim 2.3\sigma$  level compared to (Zhang et al. 2011,  $\sigma_{L_X|M_{\text{gas}}} = 0.14^{+0.02}_{-0.02}$ ), and at the  $\sim 5.4\sigma$  level relative to (Bahar et al. 2022,  $\sigma_{L_X|M_{\text{gas}}} = 0.30^{+0.02}_{-0.02}$ ). This may be attributed to the different sample sizes of galaxy groups used in the works, where feedback mechanisms can play a significant role.

#### 4.3. Soft band X-ray luminosity–Low-scatter mass proxy scaling relation

Kravtsov et al. (2006) introduced the X-ray analog of the integrated Compton- $Y$  parameter, defined as  $Y_X = M_{\text{gas}} \times T$ . This quantity is linked to the ICM’s total thermal energy and serves as a low-scatter mass proxy. Numerical simulations have demonstrated that  $Y_X$  is insensitive to the specific assumptions used in modelling feedback processes (e.g., Stanek et al. 2010). This robustness makes  $Y_X$  a reliable and consistent mass proxy that can be used in multi-wavelength studies of galaxy clusters.

Studies that have investigated the  $L_X - Y_X$  scaling relation have found deviations from self-similar expectations ( $L_X \propto Y_X^{3/5}$ ) (e.g., Maughan 2007; Pratt et al. 2009; Eckmiller et al. 2011; Lovisari et al. 2015; Bahar et al. 2022).

We find best-fit parameters for the  $L_X - Y_X$  scaling relation of  $B = 0.855^{+0.009}_{-0.009}$  for the slope,  $C = 2.09^{+0.16}_{-0.17}$  for the redshift evolution, and an intrinsic scatter of  $\sigma_{L_X|Y_X} = 0.25^{+0.01}_{-0.01}$ . The corresponding model is shown in Fig. 7. Statistically, our best-fit slope is inconsistent with the expected value at the  $\sim 28\sigma$  significance level. The redshift evolution parameter also differs from the self-similar value ( $C_{\text{SS}} = 8/5$ ), with a tension of about  $\sim 3\sigma$ . When fixing the redshift evolution to the self-similar value, the slope remains nearly unchanged at  $B = 0.866^{+0.009}_{-0.009}$ , indicating that our slope result is robust against assumptions on the redshift dependence.

These results are compared with previous studies in Fig. 8. The slope  $B$  is in agreement within  $1\sigma$  with the findings of Maughan (2007, core excised measurements), Pratt et al. (2009), and Bahar et al. (2022). A milder discrepancy is observed when compared to the results of (Eckmiller et al. 2011,  $\sim 3.4\sigma$ ) and (Lovisari et al. 2015,  $\sim 2.1\sigma$ ). A common feature among all these studies is that the measured slope is consistently steeper than the self-similar prediction. Additionally, our redshift evolution parameter value is higher than that reported by (Bahar et al. 2022,  $C = 1.50^{+0.33}_{-0.35}$ ), but it is in agreement at the  $\sim 1.5\sigma$  level. Fig. B.3 presents a comparison of our measured  $\sigma_{L_X|Y_X}$  with values reported in the literature. Our result is in strong agreement ( $1\sigma$ ) with the studies of Maughan (2007) and Bahar et al. (2022). Higher values are reported by Pratt et al. (2009), Eckmiller et al. (2011), and Lovisari et al. (2015); however, the latter two do not provide uncertainties for their measurements, making a meaningful statistical comparison with our result not possible.

#### 4.4. Gas mass–Temperature scaling relation

Another useful scaling relation for probing the total thermal energy of the ICM is the  $M_{\text{gas}} - T$  relation. As noted earlier, the temperature  $T$  reflects the average kinetic energy per particle in the ICM, while  $M_{\text{gas}}$  is proportional to the total number of particles. Together, these quantities provide a direct measurement on the ICM’s total thermal energy content, making the  $M_{\text{gas}} - T$  relation a valuable diagnostic for cluster thermodynamics and the impact of non-gravitational processes. While  $M_{\text{gas}}$  and  $T$  are linked indirectly, their shared dependence on cluster mass naturally produces a meaningful  $M_{\text{gas}} - T$  relation, combining the effects of the  $M_{\text{gas}} - M$  and  $M - T$  relations.

Studies of the  $M_{\text{gas}} - T$  relation have consistently reported a slope of around 2, significantly steeper than the self-similar expectation ( $M_{\text{gas}} \propto T^{3/2}$ , e.g., Arnaud et al. 2007; Croston et al. 2008; Zhang et al. 2008; Bahar et al. 2022). This discrepancy suggests that additional physical processes, beyond purely gravitational heating, may play a role in shaping the gas mass–temperature scaling.

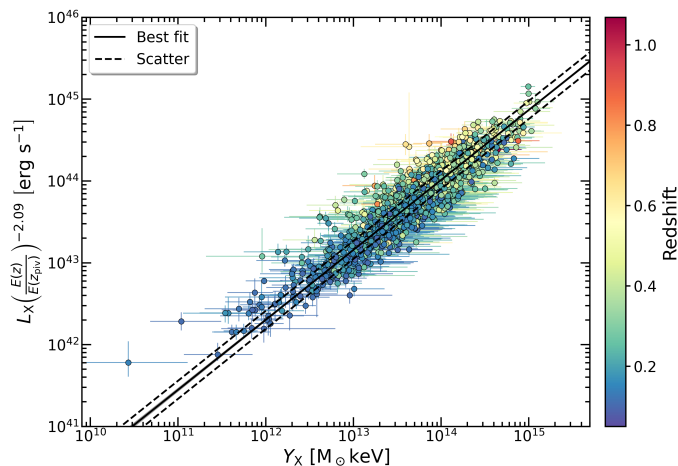


Fig. 7: Same as Fig. 3, but for soft band (0.5 – 2.0 keV energy band) X-ray luminosity–low-scatter mass proxy,  $L_X - Y_X$ , scaling relation.

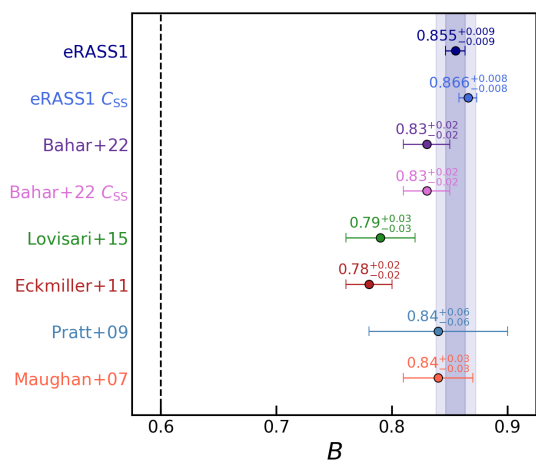


Fig. 8: Same as Fig. 4, but presenting a comparison of the slope  $B$  for the  $L_X - Y_X$  scaling relation, including results from Bahar et al. (2022, eFEDS cluster sample), Lovisari et al. (2015), Eckmiller et al. (2011), Pratt et al. (2009), and Maughan (2007).

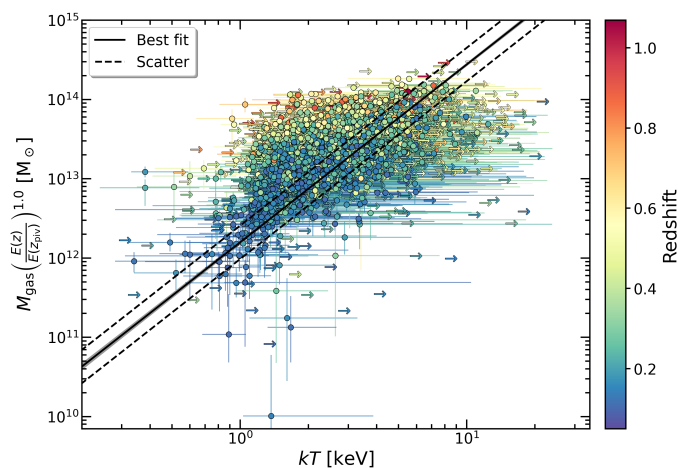


Fig. 9: Same as Fig. 3, but for Gas mass – Temperature,  $M_{\text{gas}} - T$ , scaling relation.

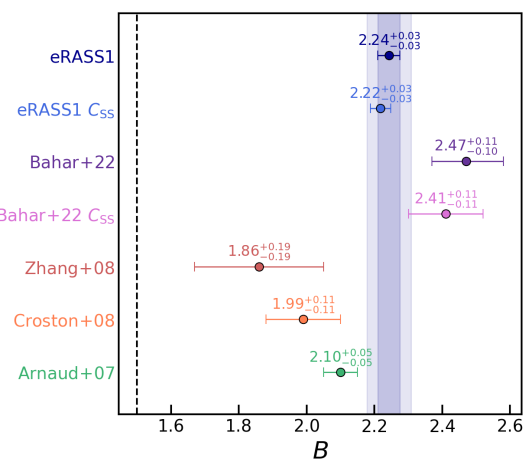


Fig. 10: Same as Fig. 4, but showing a comparison between the values of the slope  $B$  for the  $M_{\text{gas}} - T$  scaling relation, including results from Bahar et al. (2022, eFEDS cluster sample), Zhang et al. (2008), Croston et al. (2008), and Arnaud et al. (2007).

As in Bahar et al. (2022), we also adopt the  $L_X$ -based selection function by converting  $M_{\text{gas}}$  to  $L_X$ , as no simulation-derived selection function for  $M_{\text{gas}}$  is available. This one-to-one conversion should not significantly bias our results, since  $L_X$  and  $M_{\text{gas}}$  are tightly correlated with relatively low scatter (see Section 4.2).

The resulting best-fit parameters for the  $M_{\text{gas}} - T$  relation are  $B = 2.24^{+0.03}_{-0.03}$  for the slope,  $C = -1.00^{+0.29}_{-0.30}$  for the redshift evolution, and  $\sigma_{M_{\text{gas}}|T} = 0.49^{+0.02}_{-0.02}$  for the intrinsic scatter. The corresponding model is presented in Fig. 9. Our best-fit  $B$  value deviates from the self-similar one by  $\sim 25\sigma$ . However, we find that the redshift evolution parameter is strongly consistent with the self-similar expectation ( $C_{\text{SS}} = -1$ ). Fixing the redshift evolution to the self-similar value yields a slope of  $B = 2.22^{+0.03}_{-0.03}$ , nearly identical to our baseline result, indicating that the slope is robust to assumptions about redshift dependence.

Our slope  $B$  measurements are compared with earlier studies in Fig. 10. We find steeper values than those reported by Arnaud et al. (2007), Croston et al. (2008), and Zhang et al. (2008), but shallower than the results of Bahar et al. (2022). The difference appears linked to sample composition: the earlier works focused on massive, nearby clusters, whereas Bahar et al. (2022) included a much larger fraction of low-mass systems, which can strongly influence the fitted slope.

Fig. B.4 presents a comparison of our measured  $\sigma_{M_{\text{gas}}|T}$  with values reported in the literature. Zhang et al. (2008), Croston et al. (2008) and Arnaud et al. (2007) report lower values for the intrinsic scatter of the  $\sigma_{M_{\text{gas}}|T}$  relation, but these measurements are presented without error bars and therefore a statistical comparison with our findings cannot be made.

## 5. Discussion

The large sample of galaxy groups and clusters analyzed in this study enables tight constraints on the parameters describing the scaling relations, e.g., the slope, the redshift evolution parameter. The resulting uncertainties are significantly smaller than those reported in previous studies, reflecting the statistical power of the eRASS1 galaxy cluster and group sample. In the next sections we discuss the results of our analysis in more detail.

### 5.1. Deviations from self-similar predictions

The slopes,  $B$ , of the scaling relations between X-ray observables analyzed in this work exhibit statistically significant deviations from the predictions of the self-similar model, with departures exceeding  $25\sigma$ . Our results are in agreement with previous observational studies that also find a departure from the self-similar scenario (e.g., [Maughan 2007](#); [Eckmiller et al. 2011](#); [Zhang et al. 2011](#); [Kettula et al. 2015](#); [Lovisari et al. 2015](#); [Mantz et al. 2016](#); [Migkas et al. 2020](#); [Bahar et al. 2022](#)). These slope discrepancies are commonly attributed to non-gravitational processes in the ICM, such as feedback from AGN, galactic winds, and star formation (e.g., [Voit 2005](#)). Such processes inject additional energy into the ICM, altering its thermodynamic structure by heating the gas and raising its entropy, particularly in the central regions of clusters. Such mechanisms disrupt the simplifying assumptions of self-similarity, including spherical symmetry and purely gravitational heating. Theoretical studies and hydrodynamical simulations further support the breakdown of self-similarity due to these non-gravitational effects (e.g., [Babul et al. 2002](#); [Truong et al. 2018](#); [Henden et al. 2018, 2019](#)).

### 5.2. Galaxy groups in the sample

As discussed in Section 4.1, one of our main results is the discrepancy in the slope values of the  $L_X - T$  and  $L_X - M_{\text{gas}}$  relations when compared to the findings of [Bahar et al. \(2022, eFEDS sample\)](#). It has been shown that galaxy groups tend to follow a steeper  $L_X - T$  scaling relation than clusters due to the larger scatter in their ICM properties (e.g., [Maughan et al. 2012](#); [Osmond & Ponman 2004](#); [Lovisari et al. 2021](#)). In the full eRASS1 cluster catalog ([Bulbul et al. 2024](#)), the fraction of galaxy groups ( $< 10^{14} M_{\odot}$ ) is approximately 23%, indicating that the eRASS1 survey’s shallowness favors the detection of higher-mass systems. Even after decreasing the extent likelihood threshold (see Section 2.1) to enlarge our sample, the proportion of low-mass systems remains limited. For instance, selecting  $\mathcal{L}_{\text{ext}} > 7$  increases the sample size by 70% and raises the group fraction to 13%, but also increases the sample contamination to 5%. In this analysis, we prioritized maintaining low contamination to ensure the reliability of our sample and the robustness of our best-fit models. Future analysis of deeper eRASS:5 observations will improve sensitivity to low-mass systems, allowing for a better assessment of their influence on scaling relations, e.g., by allowing a broken power-law fit to the entire galaxy group and cluster sample.

A potential source of systematic uncertainty in the group results is the assumed metallicity of  $0.3 Z_{\odot}$ . If the true metallicities are higher, the inferred temperatures and luminosities could be biased low, whereas lower metallicities could bias them high. However, the magnitude of this effect is expected to be small compared to the statistical uncertainties of our measurements. For example, the median  $kT$  of our sample is 2.27 keV. For a 2.27 keV object, changing metallicity from 0.3 to  $0.4 Z_{\odot}$  only results in a  $\sim 5\%$  change in luminosity. Moreover, other mechanisms for lower mass clusters and groups, primarily line emission from collisionally excited ions, make increasingly important contributions to the overall X-ray emission ([Lovisari et al. 2021](#); [Lovisari & Maughan 2022](#)). Given the shallow nature of our X-ray data, it is not possible to determine the impact of such a mechanism on our sample, and therefore, it is referred to future work.

### 5.3. Cool-core effects

Evidence indicates that the most massive, relaxed clusters follow a self-similar  $L_X - T$  scaling relation when their cores are excluded ([Maughan et al. 2012](#)), as non-gravitational effects such as cooling and AGN feedback are minimal in the outer regions. However, we are unable to test this with our current sample for two main reasons. First, eRASS1 clusters have low photon counts, and excising the core further reduces photon statistics, often rendering X-ray measurements unreliable or unfeasible.

### 5.4. $R_{500}$ estimations

As discussed in [Lovisari et al. \(2015\)](#), steep slopes may also result from underestimated  $R_{500}$  values, due to unaccounted non-thermal pressure in hydrostatic mass estimates, which leads to lower luminosities. Temperatures are less affected due to larger uncertainties. As stated in [Bahar et al. \(2022\)](#), we also argue that the hydrostatic equilibrium bias and radius of extraction do not have an impact on the results of this study. As mentioned in Section 2.2, the  $M_{500}$ , and therefore  $R_{500}$ , estimates come from the scaling relations between weak lensing shear data and X-ray count rate.

### 5.5. Selection biases

Selection biases, such as the Malmquist bias, arising because brighter sources are detectable at greater distances ([Malmquist 1922](#)), are a common concern in studies of astrophysical samples, especially flux-limited samples. In our analysis, these effects are carefully modeled and included through the selection function. The determination of the selection function for the eRASS1 sample ([Clerc et al. 2024](#)) builds upon and improves the method used in the eFEDS analysis ([Bahar et al. 2022](#)). The selection function has been carefully modeled and tested on end-to-end simulations of the eROSITA sky, which include a realistic, representative distribution of galaxy groups and clusters ([Comparat et al. 2020](#); [Seppi et al. 2022](#)). Its reliability has been demonstrated in recent cosmological constraints from eROSITA cluster abundances ([Ghirardini et al. 2024](#)). We therefore conclude that the observed departures from self-similar scaling in our results cannot be attributed to selection biases.

There is evidence that relaxed, cool-core clusters exhibit less scatter in scaling relations than mergers ([Vikhlinin et al. 2009](#); [Mantz et al. 2010](#)), and reducing scatter is crucial for tightening cosmological constraints from cluster counts. [Sanders \(A&A submitted 2025\)](#) recently derived the intrinsic distribution of eRASS1 morphological parameters within a Bayesian framework, constructed their scaling relations with redshift and luminosity, and examined their distributions in redshift and luminosity bins. These results provide a basis for future analyses employing morphology-based selection functions and dynamical-state-dependent mass functions to study X-ray scaling relations between observables.

### 5.6. Temperature offsets

Previous studies comparing eROSITA with XMM-Newton and Chandra have found inconsistent temperature offsets, with results ranging from eROSITA measuring lower ( $> 25\%$ ) to slightly higher temperatures depending on the studied cluster, chosen energy band, and observation mode, pointed observation or survey ([Sanders et al. 2022](#); [Whelan et al. 2022](#); [Veronica et al. 2022](#); [Liu et al. 2023](#)). These works relied on single-

cluster analyses, which are prone to noise and methodological differences, such as varying metal abundances and Galactic absorption assumptions. Turner et al. (2022) analyzed eight eFEDS clusters and found eROSITA temperatures  $25 \pm 9\%$  lower than XMM-Newton in the broad band, though different energy bands were used. Migkas et al. (2024) recently compared eROSITA galaxy cluster temperatures with those from Chandra and XMM-Newton using a large sample. They measured 186 overlapping regions ( $< R_{500}$ ) with Chandra and 71 with XMM-Newton in the full (0.7 – 7.0 keV), soft (0.5 – 4.0 keV), and hard (1.5 – 7 keV) X-ray energy bands. eROSITA temperatures were consistently lower, by 15 – 38% depending on cluster temperature and energy band, with the largest differences for hot clusters, smaller offsets for cool systems, and the strongest mismatch in the hard band. A broken power-law fit showed a break in the scaling relation around 1.7 – 2.7 keV, depending on the energy band. These results may suggest that our best-fit  $L_X - T$  and  $M_{\text{gas}} - T$  relations are steeper than the self-similar expectation because hotter systems are in reality cooler. Nonetheless, our findings agree with previous scaling relation studies, mostly based on Chandra and XMM-Newton data, which also report steeper  $L_X - T$  and  $M_{\text{gas}} - T$  relations than predicted by the self-similar model (e.g., Arnaud et al. 2007; Pratt et al. 2009; Eckmiller et al. 2011; Kettula et al. 2015; Lovisari et al. 2015; Giles et al. 2016; Migkas et al. 2020). The eRASS1 cluster temperatures were derived using MBProj2D in the 0.3 – 7.0 keV energy band (see Section 2.2, and Bulbul et al. 2024), whereas the closest correction available in Migkas et al. (2024) corresponds to the full band (0.7 – 7.0 keV), which omits the 0.3 – 0.7 keV energy band, removing an important part of the eROSITA sensitive energy band for cluster analysis. Furthermore, about  $\sim 54\%$  of our selected clusters lack well-constrained temperatures in Bulbul et al. (2024), having only upper or lower limits due to the shallow nature of eRASS1 observations. While this is not an issue for our scaling relation fitting (which uses the full temperature posterior distributions; see Section 3.2), only  $\sim 46\%$  of our sample has constrained temperatures, and just 85 systems have relative uncertainties below  $< 20\%$ . Despite these limitations, we applied the eROSITA–XMM-Newton temperature relation from Migkas et al. (2024), converting our temperature chains and fitting the  $L_X - T$  relation. We obtain a slope of  $B = 2.47_{-0.04}^{+0.04}$ , a redshift evolution parameter of  $C = 1.25_{-0.53}^{+0.53}$ , and an intrinsic scatter of  $\sigma_{L_X|T} = 0.65_{-0.03}^{+0.03}$ . The slope is consistent with our results in Section 4.1, while the redshift evolution is somewhat lower, but still compatible within uncertainties. The intrinsic scatter increases, which can be attributed to the additional uncertainties introduced by the temperature offset, in addition with the existing measurement errors.

### 5.7. Redshift evolution

Understanding the scaling relation redshift evolution is essential for cosmological uses of clusters. However, this has been a challenging task due to the lack of high-quality data for large, well-characterized samples of high-redshift clusters, and the need for a consistent low-redshift counterpart. Differences in sample selection, analysis, or instrumentation between local and distant data can hide or mimic a plausible evolution. Giodini et al. (2013) and Lovisari & Maughan (2022) note that there is still no clear consensus in the literature regarding the redshift evolution of scaling relations, despite numerous past studies. The sample of Bahar et al. (2022), covering  $0.017 < z < 0.940$ , shows self-similar redshift evolution for all examined scaling relations (the

same as those in this work) at a significance below  $2.5\sigma$ . Similarly, we find only mild evolution, consistent with self-similar predictions at the  $1 - 3\sigma$  confidence level.

Our results show no significant deviation from self-similar expectations in the evolution of galaxy cluster scaling relations out to  $z \sim 1.2$ , suggesting that clusters formed or reached equilibrium relatively recently compared to the epoch of observation. However, uncertainties remain, and both weaker and stronger departures from self-similar predictions cannot yet be ruled out.

### 5.8. Intrinsic scatter

As mentioned in Lovisari et al. (2021), scaling relations deviate from self-similar predictions partly due to their intrinsic scatter. In relations involving  $L_X$ , the scatter can be as large as 50 – 70% at a fixed  $T$  (see Fig. B.1). Our results for this relation give an intrinsic scatter of  $\sim 77\%$ . Previous studies (e.g., Maughan 2007) have shown that this large variation is mainly caused by the cluster cores, where cool-core systems show enhanced luminosities. Excluding the central  $0.15R_{500}$ , for example, reduces the intrinsic scatter to 10 – 20%. However, excluding the central part of eRASS1 systems is not possible with current data (see Section 5.3).

For the other scaling relations presented in this work, however, the situation is less clear. Reported scatter values in the literature span a broad range, often depending on sample selection, measurement methods, etc. Some studies do report errors on their scatter, while others report substantially larger scatter, reflecting both astrophysical diversity among clusters and systematic differences in analysis. As a result, a direct comparison with our findings is not straightforward.

## 6. Summary

We use the largest ICM/IGrM-detected sample of galaxy groups and clusters to date from the eRASS1 catalogue to investigate the X-ray scaling relations  $L_X - T$ ,  $L_X - M_{\text{gas}}$ ,  $L_X - Y_X$ , and  $M_{\text{gas}} - T$ . The sample comprises 3061 objects spanning  $0.05 < z < 1.07$  and  $1.1 \times 10^{13} < M_{500}/M_{\odot} < 1.6 \times 10^{15}$ . Our analysis includes a detailed treatment of the cluster selection function. We fit the scaling relations, allowing the normalization, slope, redshift evolution, and intrinsic scatter in both  $X$  and  $Y$  to vary freely. In a second run, the redshift evolution exponent was fixed to the corresponding self-similar value. Our results are summarized as follows:

- The slopes of the X-ray scaling relations studied here deviate significantly from self-similar expectations, but are consistent with previously reported observational and simulation results. Our findings support the interpretation that these departures from self-similarity arise from non-gravitational processes, such as feedback mechanisms.
- With the large sample of groups and clusters analyzed here, we robustly confirm that the redshift evolution of the X-ray scaling relations remains broadly consistent with the self-similar model out to  $z \sim 1.2$ . When the evolution exponent is fixed to its self-similar value, the best-fit slopes change by less than  $1\sigma$  relative to the free-exponent case.
- The intrinsic scatter of the  $L_X - T$  relation is consistent with values reported in previous studies, confirming agreement with earlier observational constraints. For the other scaling relations, however, the wide range of scatter values found in the literature makes direct comparison less straightforward. In all cases, the level of scatter remains similar in both cases,

whether the redshift evolution parameter is left free or fixed to the self-similar value, suggesting that our inference of scatter is robust against assumptions about the redshift dependence.

- Compared to the eFEDS sample analyzed in Bahar et al. (2022), our galaxy group and cluster sample contains relatively fewer low-mass systems, which may account for the discrepancy in slope values. Future, larger samples of groups and clusters from deeper data will provide a clearer understanding of the impact of galaxy groups on scaling relation fits.

Even with shallow observations, eROSITA has successfully imaged hundreds of galaxy clusters and groups and enabled robust measurements of their X-ray properties, even from only a few photons. Our work demonstrates that those results can place tight constraints on the X-ray scaling relations of clusters and groups. With future, deeper eROSITA catalogs, the significantly increased number of detected systems, particularly at the group scale, will allow us to extend these constraints to lower masses and redshifts. This will provide a unique opportunity to probe the interplay of gravitational and non-gravitational processes in structure formation, thereby deepening our understanding of the physics that governs the evolution of galaxy groups and clusters.

*Acknowledgements.* This work is based on data from eROSITA, the soft X-ray instrument aboard SRG, a joint Russian-German science mission supported by the Russian Space Agency (Roskosmos), in the interests of the Russian Academy of Sciences represented by its Space Research Institute (IKI), and the Deutsches Zentrum für Luft und Raumfahrt (DLR). The SRG spacecraft was built by the Lavochkin Association (NPOL) and its subcontractors and is operated by NPOL with support from the Max Planck Institute for Extraterrestrial Physics (MPE). The development and construction of the eROSITA X-ray instrument were led by MPE, with contributions from the Dr. Karl Remeis Observatory Bamberg & ECAP (FAU Erlangen-Nuernberg), the University of Hamburg Observatory, the Leibniz Institute for Astrophysics Potsdam (AIP), and the Institute for Astronomy and Astrophysics of the University of Tübingen, with the support of DLR and the Max Planck Society. The Argelander Institute for Astronomy of the University of Bonn and the Ludwig Maximilians Universität Munich also participated in the science preparation for eROSITA.

The eROSITA data shown here were processed using the eSASS/NRTA software system developed by the German eROSITA consortium.

E. Bulbul, S. Zelmer, X. Zhang, and E. Artis acknowledge financial support from the European Research Council (ERC) Consolidator Grant under the European Union's Horizon 2020 research and innovation program (grant agreement CoG DarkQuest No 101002585). N. Clerc was financially supported by CNES. A. Liu acknowledges the support from the National Natural Science Foundation of China (Grant No. 12588202). A. Liu is supported by the China Manned Space Program with grant no. CMS-CSST-2025-A04.

This work made use of SciPy (Jones et al. 2001), matplotlib, a Python library for publication-quality graphics (Hunter 2007), Astropy, a community-developed core Python package for Astronomy (Astropy Collaboration et al. 2013), NumPy (Van Der Walt et al. 2011), Colossus (Diemer 2018), and ChainConsumer (Hinton 2016).

## References

Allen, S. W., Evrard, A. E., & Mantz, A. B. 2011, *ARA&A*, 49, 409  
 Arnaud, M., Pointecouteau, E., & Pratt, G. W. 2007, *A&A*, 474, L37  
 Asplund, M., Grevesse, N., Sauval, A. J., & Scott, P. 2009, *ARA&A*, 47, 481  
 Astropy Collaboration, Robitaille, T. P., Tollerud, E. J., et al. 2013, *A&A*, 558, A33  
 Babul, A., Balogh, M. L., Lewis, G. F., & Poole, G. B. 2002, *MNRAS*, 330, 329  
 Bahar, Y. E., Bulbul, E., Clerc, N., et al. 2022, *A&A*, 661, A7  
 Bahar, Y. E., Bulbul, E., Ghirardini, V., et al. 2024, *A&A*, 691, A188  
 Balzer, F., Bulbul, E., Kluge, M., et al. 2025, *A&A*, 701, A283  
 Barnes, D. J., Kay, S. T., Henson, M. A., et al. 2017, *MNRAS*, 465, 213  
 Brunner, H., Liu, T., Lamer, G., et al. 2022, *A&A*, 661, A1  
 Bulbul, E., Chiu, I. N., Mohr, J. J., et al. 2019, *ApJ*, 871, 50  
 Bulbul, E., Liu, A., Kluge, M., et al. 2024, *A&A*, 685, A106  
 Chiu, I. N., Ghirardini, V., Liu, A., et al. 2022, *A&A*, 661, A11  
 Churazov, E., Forman, W., Jones, C., Sunyaev, R., & Böhringer, H. 2004, *MNRAS*, 347, 29

Clerc, N., Comparat, J., Seppi, R., et al. 2024, *A&A*, 687, A238  
 Comparat, J., Eckert, D., Finoguenov, A., et al. 2020, *The Open Journal of Astrophysics*, 3, 13  
 Croston, J. H., Pratt, G. W., Böhringer, H., et al. 2008, *A&A*, 487, 431  
 Diemer, B. 2018, *ApJS*, 239, 35  
 Eckmiller, H. J., Hudson, D. S., & Reiprich, T. H. 2011, *A&A*, 535, A105  
 Ettori, S., Tozzi, P., Borgani, S., & Rosati, P. 2004, *A&A*, 417, 13  
 Fabian, A. C. 2012, *ARA&A*, 50, 455  
 Foreman-Mackey, D., Hogg, D. W., Lang, D., & Goodman, J. 2013, *PASP*, 125, 306  
 Freyberg, M., Perinati, E., Pacaud, F., et al. 2021, in *Society of Photo-Optical Instrumentation Engineers (SPIE) Conference Series*, Vol. 11444, Society of Photo-Optical Instrumentation Engineers (SPIE) Conference Series, ed. J.-W. A. den Herder, S. Nikzad, & K. Nakazawa, 1144410  
 Ghirardini, V., Bulbul, E., Artis, E., et al. 2024, *A&A*, 689, A298  
 Ghirardini, V., Bulbul, E., Hoang, D. N., et al. 2021, *A&A*, 647, A4  
 Giles, P. A., Maughan, B. J., Pacaud, F., et al. 2016, *A&A*, 592, A3  
 Giodini, S., Lovisari, L., Pointecouteau, E., et al. 2013, *Space Sci. Rev.*, 177, 247  
 Gitti, M., Brighenti, F., & McNamara, B. R. 2012, *Advances in Astronomy*, 2012, 950641  
 Grandis, S., Ghirardini, V., Bocquet, S., et al. 2024, *A&A*, 687, A178  
 Henden, N. A., Puchwein, E., Shen, S., & Sijacki, D. 2018, *MNRAS*, 479, 5385  
 Henden, N. A., Puchwein, E., & Sijacki, D. 2019, *MNRAS*, 489, 2439  
 HI4PI Collaboration, Ben Bekhti, N., Flöer, L., et al. 2016, *A&A*, 594, A116  
 Hilton, M., Romer, A. K., Kay, S. T., et al. 2012, *MNRAS*, 424, 2086  
 Hinton, S. R. 2016, *The Journal of Open Source Software*, 1, 00045  
 Hunter, J. D. 2007, *Computing In Science & Engineering*, 9, 90  
 Ider Chitham, J., Comparat, J., Finoguenov, A., et al. 2020, *MNRAS*, 499, 4768  
 Jones, E., Oliphant, T., Peterson, P., et al. 2001, *SciPy: Open source scientific tools for Python*  
 Kaiser, N. 1986, *MNRAS*, 222, 323  
 Kettula, K., Giodini, S., van Uitert, E., et al. 2015, *MNRAS*, 451, 1460  
 Kleinebreil, F., Grandis, S., Schrabback, T., et al. 2024, *arXiv e-prints*, arXiv:2402.08456  
 Kluge, M., Comparat, J., Liu, A., et al. 2024, *A&A*, 688, A210  
 Kravtsov, A. V. & Borgani, S. 2012, *ARA&A*, 50, 353  
 Kravtsov, A. V., Vikhlinin, A., & Nagai, D. 2006, *ApJ*, 650, 128  
 Liu, A., Bulbul, E., Ghirardini, V., et al. 2022, *A&A*, 661, A2  
 Liu, A., Bulbul, E., Ramos-Ceja, M. E., et al. 2023, *A&A*, 670, A96  
 Lovisari, L., Ettori, S., Gaspari, M., & Giles, P. A. 2021, *Universe*, 7, 139  
 Lovisari, L. & Maughan, B. J. 2022, in *Handbook of X-ray and Gamma-ray Astrophysics*, ed. C. Bambi & A. Sanganello, 65  
 Lovisari, L., Reiprich, T. H., & Schellenberger, G. 2015, *A&A*, 573, A118  
 Malmquist, K. G. 1922, *Meddelanden fran Lunds Astronomiska Observatorium Serie 1*, 100, 1  
 Mantz, A., Allen, S. W., Rapetti, D., & Ebeling, H. 2010, *MNRAS*, 406, 1759  
 Mantz, A. B., Allen, S. W., Morris, R. G., et al. 2016, *MNRAS*, 463, 3582  
 Markevitch, M. 1998, *ApJ*, 504, 27  
 Maughan, B. J. 2007, *ApJ*, 668, 772  
 Maughan, B. J., Giles, P. A., Randall, S. W., Jones, C., & Forman, W. R. 2012, *MNRAS*, 421, 1583  
 McNamara, B. R. & Nulsen, P. E. J. 2007, *ARA&A*, 45, 117  
 Menci, N. & Cavaliere, A. 2000, *MNRAS*, 311, 50  
 Merloni, A., Lamer, G., Liu, T., et al. 2024, *arXiv e-prints*, arXiv:2401.17274  
 Merloni, A., Predehl, P., Becker, W., et al. 2012, *arXiv e-prints*, arXiv:1209.3114  
 Migkas, K., Kox, D., Schellenberger, G., et al. 2024, *A&A*, 688, A107  
 Migkas, K., Schellenberger, G., Reiprich, T. H., et al. 2020, *A&A*, 636, A15  
 Okabe, N., Reiprich, T., Grandis, S., et al. 2025, *arXiv e-prints*, arXiv:2503.09952  
 Osmond, J. P. F. & Ponman, T. J. 2004, *MNRAS*, 350, 1511  
 Pacaud, F., Clerc, N., Giles, P. A., et al. 2016, *A&A*, 592, A2  
 Planck Collaboration, Ade, P. A. R., Aghanim, N., et al. 2013, *A&A*, 550, A130  
 Planck Collaboration, Ade, P. A. R., Aghanim, N., et al. 2016, *A&A*, 594, A27  
 Pratt, G. W., Arnaud, M., Biviano, A., et al. 2019, *Space Sci. Rev.*, 215, 25  
 Pratt, G. W., Croston, J. H., Arnaud, M., & Böhringer, H. 2009, *A&A*, 498, 361  
 Predehl, P., Andriutschke, R., Arefiev, V., et al. 2021, *A&A*, 647, A1  
 Ramos-Ceja, M. E., Oguri, M., Miyazaki, S., et al. 2022, *A&A*, 661, A14  
 Reichardt, C. L., Stalder, B., Bleem, L. E., et al. 2013, *ApJ*, 763, 127  
 Reiprich, T. H. & Böhringer, H. 2002, *ApJ*, 567, 716  
 Sanders, J. *A&A* submitted 2025, *Journal Name*, in prep.  
 Sanders, J. S., Biffi, V., Brügggen, M., et al. 2022, *A&A*, 661, A36  
 Sanders, J. S., Fabian, A. C., Russell, H. R., & Walker, S. A. 2018, *MNRAS*, 474, 1065  
 Seppi, R., Comparat, J., Bulbul, E., et al. 2022, *A&A*, 665, A78  
 Stanek, R., Rasia, E., Evrard, A. E., Pearce, F., & Gazzola, L. 2010, *ApJ*, 715, 1508  
 Sun, M., Voit, G. M., Donahue, M., et al. 2009, *ApJ*, 693, 1142  
 Sunyaev, R., Arefiev, V., Babushkin, V., et al. 2021, *A&A*, 656, A132  
 Tinker, J., Kravtsov, A. V., Klypin, A., et al. 2008, *ApJ*, 688, 709  
 Tozzi, P. & Norman, C. 2001, *ApJ*, 546, 63  
 Truong, N., Rasia, E., Mazzotta, P., et al. 2018, *MNRAS*, 474, 4089  
 Turner, D. J., Giles, P. A., Romer, A. K., et al. 2022, *MNRAS*, 517, 657  
 Van Der Walt, S., Colbert, S. C., & Varoquaux, G. 2011, *Computing in Science & Engineering*, 13, 22  
 Veronica, A., Su, Y., Biffi, V., et al. 2022, *A&A*, 661, A46  
 Vikhlinin, A., Burenin, R. A., Ebeling, H., et al. 2009, *ApJ*, 692, 1033  
 Vikhlinin, A., Kravtsov, A., Forman, W., et al. 2006, *ApJ*, 640, 691  
 Voit, G. M. 2005, *Reviews of Modern Physics*, 77, 207  
 Whelan, B., Veronica, A., Pacaud, F., et al. 2022, *A&A*, 663, A171  
 Willingale, R., Starling, R. L. C., Beardmore, A. P., Tanvir, N. R., & O'Brien, P. T. 2013, *MNRAS*, 431, 394  
 Zhang, Y. Y., Andernach, H., Caretta, C. A., et al. 2011, *A&A*, 526, A105  
 Zhang, Y. Y., Finoguenov, A., Böhringer, H., et al. 2008, *A&A*, 482, 451  
 Zhuravleva, I., Churazov, E., Schekochihin, A. A., et al. 2014, *Nature*, 515, 85

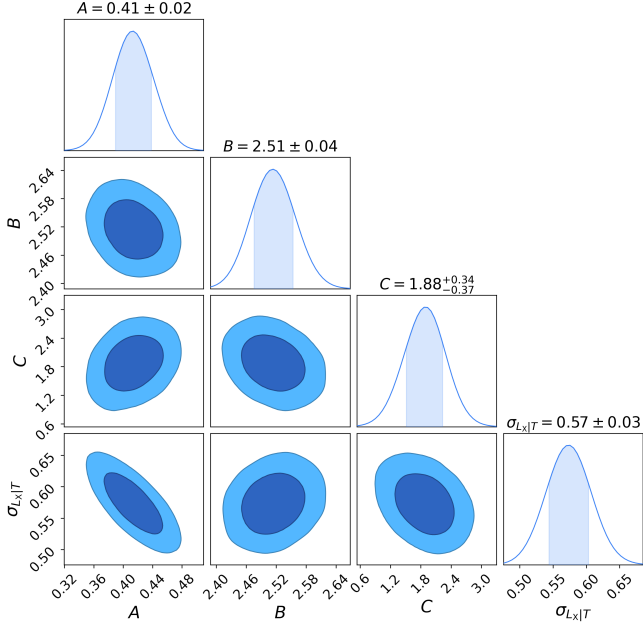


Fig. A.1: Parameter constraints of the  $L_X - T$  scaling relation. The off-diagonal panels display the joint posteriors, with contours representing the 68% (dark blue) and 95% (light blue) confidence levels. The diagonal panels show the marginalized posterior distributions, and the shaded light blue areas show the  $1\sigma$  region.

## Appendix A: Parameter constraints

Corner plots displaying the parameter distributions from the MCMC chains are shown in Figs. A.1, A.2, and A.4, for the  $L_X - T$ ,  $L_X - M_{\text{gas}}$  and  $L_X - Y_X$  scaling relation analysis, respectively. These plots show the marginalized and joint posterior distributions of the model parameters for the scaling relation fittings.

## Appendix B: Scatter comparison

Figures B.1, B.2, and B.3 display a comparison between our best-fit intrinsic scatter results with previous studies, for the  $L_X - T$ ,  $L_X - M_{\text{gas}}$  and  $L_X - Y_X$  scaling relation analysis, respectively.

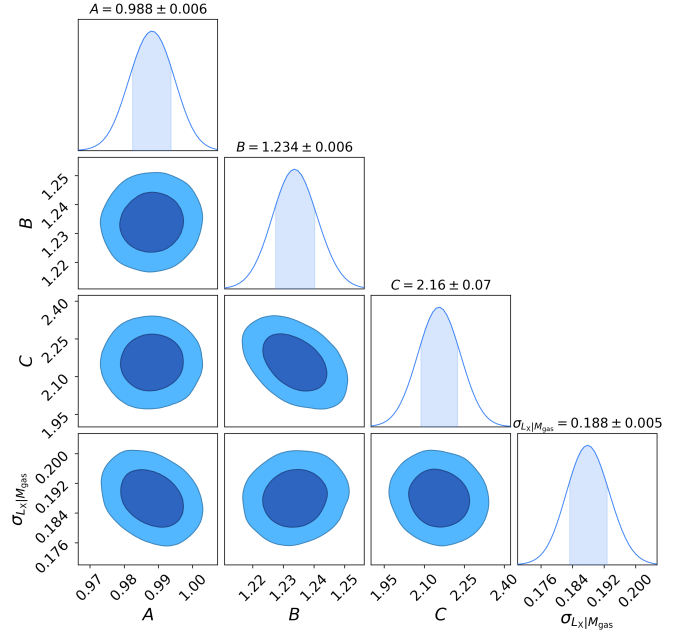


Fig. A.2: Same as Fig. A.1, but for the  $L_X - M_{\text{gas}}$  scaling relation.

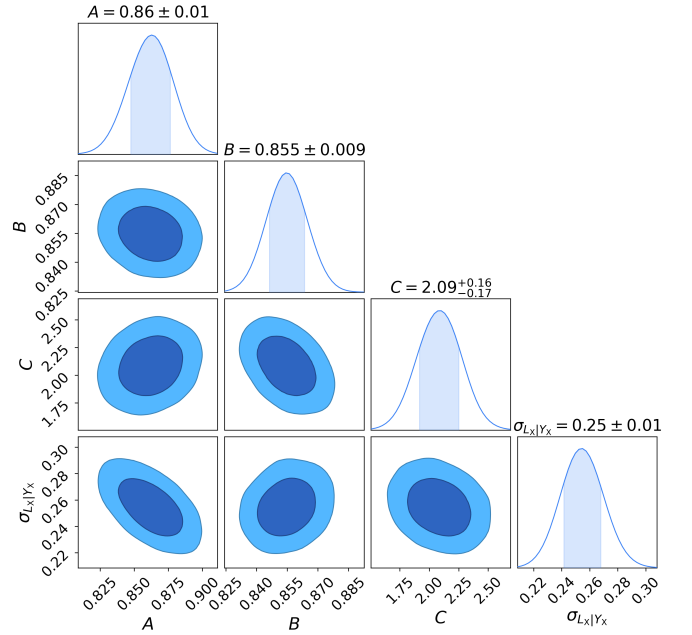
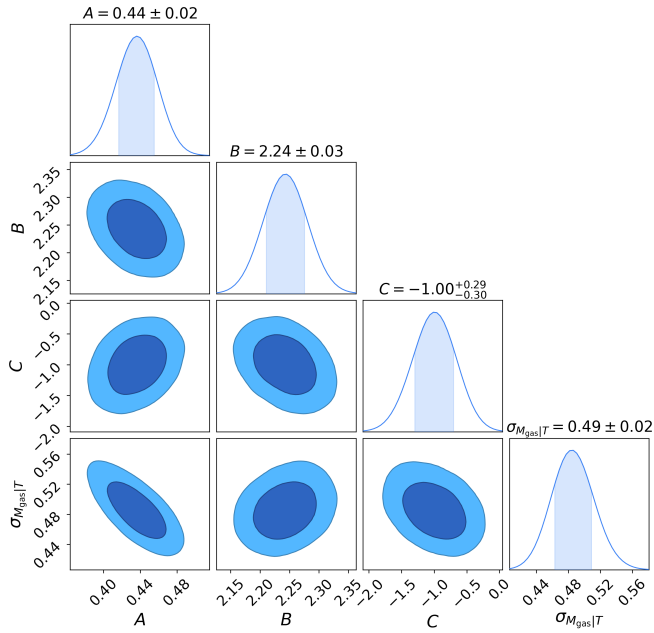
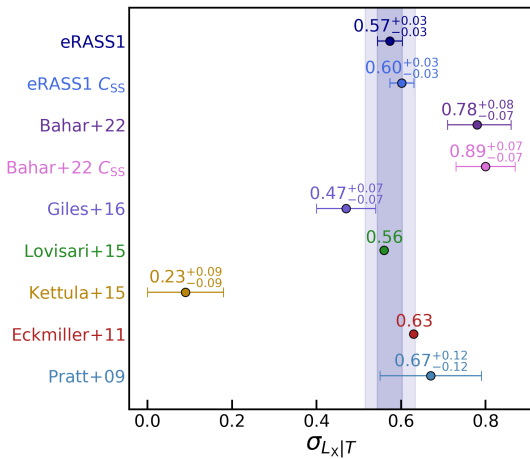
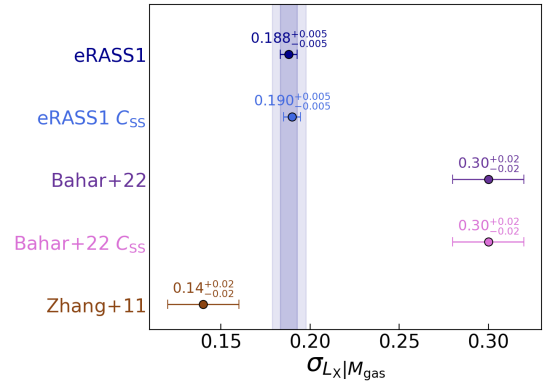
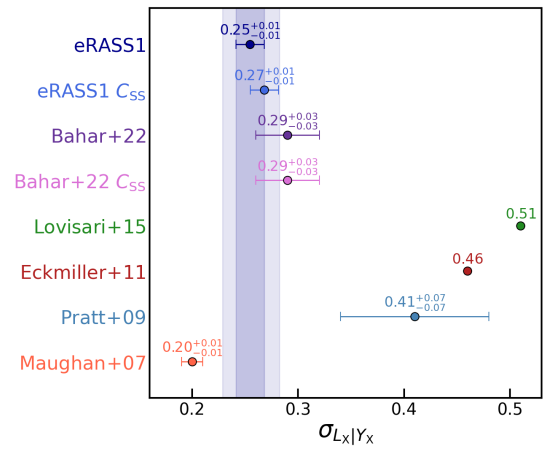
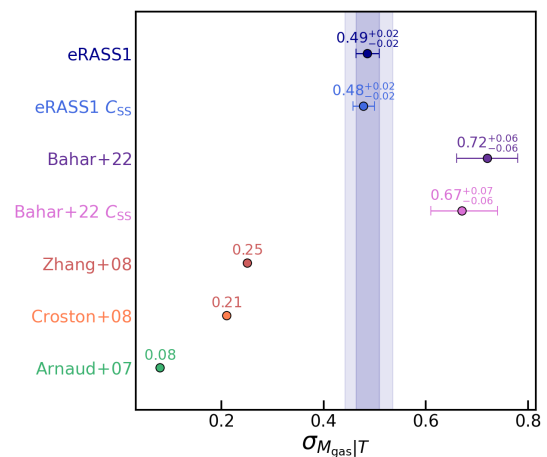


Fig. A.3: Same as Fig. A.1 but for the  $L_X - Y_X$  scaling relation.


 Fig. A.4: Same as Fig. A.1 but for the  $M_{\text{gas}} - T$  scaling relation.

 Fig. B.1: Comparison of the intrinsic scatter  $\sigma_{L_X|T}$  for the  $L_X - T$  scaling relation with literature results from Bahar et al. (2022, eFEDS cluster sample), Giles et al. (2016, XXL cluster sample), Lovisari et al. (2015), Kettula et al. (2015), Eckmiller et al. (2011), and Pratt et al. (2009). All the shown errors are at the  $1\sigma$  level. The vertical shaded areas represent our best-fit measurements at the  $1 - 2\sigma$  confidence level.

 Fig. B.2: Same as Fig. B.1, but presenting a comparison of the intrinsic scatter  $\sigma_{L_X|M_{\text{gas}}}$  for the  $L_X - M_{\text{gas}}$  scaling relation, including results from Bahar et al. (2022, eFEDS cluster sample) and Zhang et al. (2011).

 Fig. B.3: Same as Fig. B.1, but showing a comparison of the intrinsic scatter  $\sigma_{L_X|Y_X}$  for the  $L_X - Y_X$  scaling relation, including results from Bahar et al. (2022, eFEDS cluster sample), Lovisari et al. (2015), Eckmiller et al. (2011), Pratt et al. (2009), and Maughan (2007).

 Fig. B.4: Same as Fig. B.1, but showing a comparison of the intrinsic scatter  $\sigma_{M_{\text{gas}}|T}$  for the  $M_{\text{gas}} - T$  scaling relation, including results from Bahar et al. (2022, eFEDS cluster sample), Zhang et al. (2008), Croston et al. (2008), and Arnaud et al. (2007).